Single-cell-scale spatial transcriptome of the developing and adult mouse ovary

Anthony S. Martinez[#], Tyler J. Gibson[#], Jennifer McKey*

Section of Developmental Biology, Department of Pediatrics, University of Colorado Anschutz Medical Campus, Aurora, CO, USA.

[#]Authors contributed equally to this work.

*Corresponding author: jennifer.mckey@cuanschutz.edu

Abstract

Mammalian ovary development is essential for female fertility, involving the complex spatial patterning of diverse cell types to establish the finite reserve of ovarian follicles. While single-cell transcriptome analyses have provided important insights into the mechanisms driving specification and developmental trajectories of ovarian cells, they disrupt this crucial spatial context. To overcome this limitation, we used 10X Genomics Visium HD spatial transcriptomics to analyze the developing mouse ovary while maintaining its native cellular architecture. We captured all ovarian cell types at eight key fetal and postnatal timepoints, generating a near single cell resolution library of spatial gene expression across ovarian development. This comprehensive dataset allows analysis of dynamic transcriptional signatures associated with unique spatial patterning throughout development, including the establishment of cortex and medulla and assembly of ovarian follicles in each region. This dataset represents a fundamental resource for the investigation of regulatory mechanisms driving spatial patterning of the ovary and opens new avenues to explore the spatial determinants of female fertility and reproductive longevity.

Short narrative

This report describes a near-single-cell map of spatially resolved gene expression in the developing mouse ovary using 10X Genomics Visium HD, preserving the crucial cellular architecture that is lost in traditional single-cell analyses. This comprehensive dataset, covering eight key developmental timepoints, provides a fundamental resource for investigating how spatial patterning regulates critical ovarian events like follicle assembly.

Background and Summary

During fetal development, the gonad first arises as a bipotential primordium that is colonized by migrating primordial germ cells[1–6]. At the stage of sex determination, around embryonic day (E)11.5 in mice, gonads in XX embryos commit to a female fate and develop into ovaries[3,7,8]. This coincides with mitotic proliferation of germ cells that undergo incomplete cytokinesis to form germline cysts[9–11], and differentiation of bipotential supporting cells into pre-granulosa cells[3,12–15]. By E14.5 germline cysts are surrounded by pre-granulosa cells, forming transient structures termed ovigerous cords (OC) anchored in the center of the ovary[16,17]. Around E17.5, OCs begin to break down to form individual ovarian follicles defined by the assembly of one oocyte and 2-3 pre-granulosa cells[18–21]. These first follicles are assembled in the ovarian medulla with pre-granulosa cells derived from the initial pool of pre-supporting cells derived from the bipotential progenitors of the coelomic epithelium[21,22]. In the meantime, pre-granulosa cells derived from the ovarian surface epithelium after sex determination assemble with oocytes in the ovarian cortex to form cortical follicles [21,23–26]. The regionalization of follicles into cortical and medullary pools holds functional significance, as from postnatal day 2 (P2) to P7, follicles located in the medulla activate and begin to synchronously grow in a process termed first wave folliculogenesis[15,27–29]. These perinatally-activated medullary follicles are largely depleted by the onset of puberty and only represent a minor contribution to female fertility[23,28,30]. The depletion of medullary follicles leaves a significantly larger pool of quiescent follicles in the cortex that constitute the ovarian reserve

responsible for female fertility. It is from this pool, at the onset of puberty, that cyclical recruitment and ovulation of oocytes will occur[21,28,29]. Because this pool is finite, the size of the ovarian reserve at puberty and the rate of cyclical reduction are major contributors to female reproductive longevity.

Recent single cell/nucleus transcriptomic studies have allowed better appreciation of the temporal dynamics of gene expression networks during differentiation of ovarian cell types[12,22,31–36]. While these methodologies have revealed transcriptional signatures and gene regulatory networks underlying ovarian development, they disrupt the spatial organization of the tissue, limiting our understanding of the functional links between spatial patterning of ovarian cell subtypes throughout development and changes in transcriptional output. In fact, recent 3D-imaging studies of ovary morphogenesis have highlighted the spatially dynamic nature of ovarian differentiation and establishment of the ovarian reserve[7,26,29,37–40]. For example, we now know that meiotic entry of oocytes follows an anterior-posterior and radial pattern[38], that regionalization of the ovary into cortex and medulla coincides with physical folding of the ovarian domain[26], and that medullary follicles activate first in the dorsal region of the ovary during first wave folliculogenesis[29].

To begin to understand how the gene expression networks driving molecular differentiation of ovarian cells integrate spatial cues to give rise to these discrete spatiotemporal patterns, we performed genome-wide spatial profiling of gene expression across the ovary throughout development. We used 10X Genomics Visium HD technology to produce a near single-cell resolution spatial transcriptomic time course using mouse ovaries at four fetal and four postnatal timepoints. Embryonic timepoints of E12.5, E14.5, E16.5, and E18.5 were selected for their overlap with key stages of ovary morphogenesis, while postnatal timepoints of P0, P3, P21, and P90 were selected for their overlap with first wave folliculogenesis and pre- and post-pubertal states.

This dataset illustrates the spatial patterning of the ovary through the lens of gene expression and allows contextual access to the molecular mechanisms controlling the establishment and regulation of the ovarian reserve. This study paves the way towards identifying novel determinants of female fertility and reproductive longevity and will undoubtedly yield novel insight into the developmental origins of ovarian health and disease.

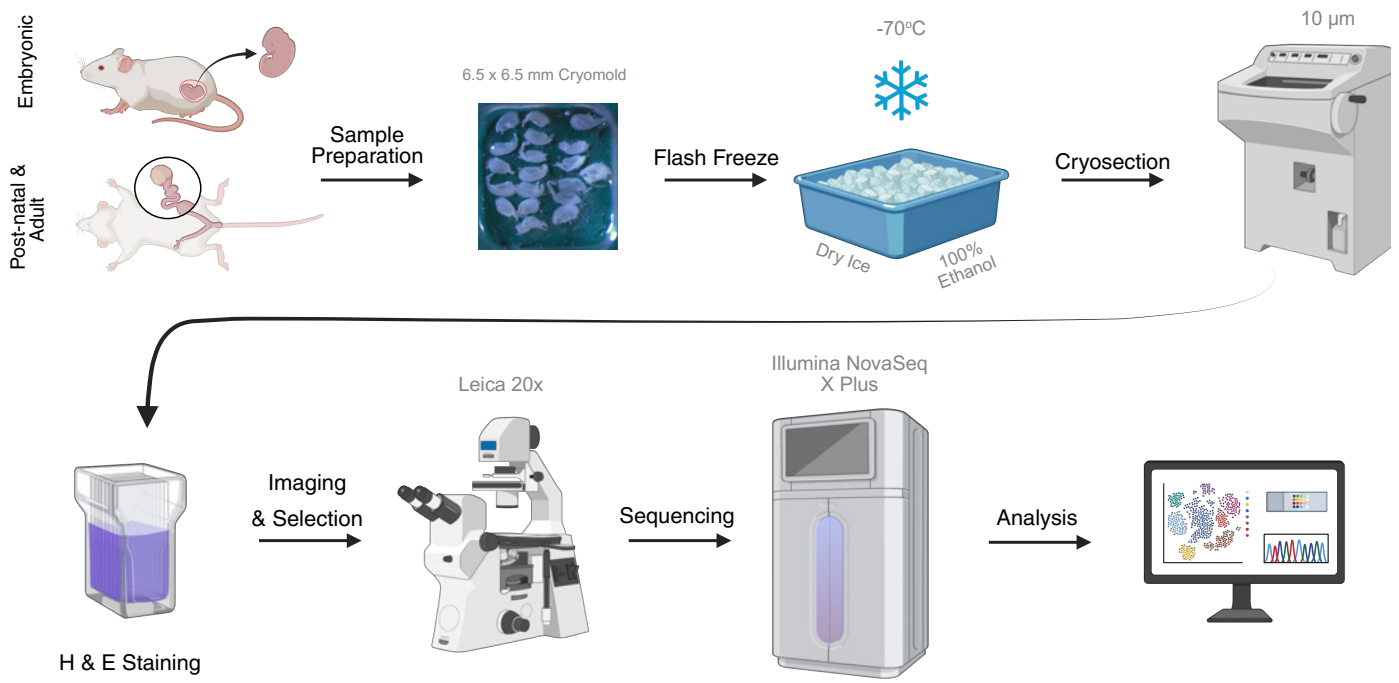

Figure 1. **Experimental design**. Fetal, postnatal, and adult ovaries were dissected, embedded in a 7 x 7 cryomold, flash frozen, and cryosectioned.10 µm sections were stained with H & E, imaged, processed for Visium HD RNA capture using CytAssist followed by cDNA library production and sequencing. Data were processed, analyzed and projected onto the H&E images using 8 µm square bin resolution. Created in BioRender. Martinez, A. (2025) https://BioRender.com/sytaju5

Methods

Mice. Outbred CD-1 mice were obtained from Charles River, Inc. (USA) and bred in our colony to produce all timepoints in this dataset. To collect ovarian tissue at specific developmental stages, triad timed matings were set up using a single male and two two-month-old virgin females. Timed-mated dams were checked every morning for vaginal plugs. The date of vaginal plug was treated as embryonic (E) day 0.5. Mice were housed in an AALAC-accredited barrier facility at the University of Colorado Anschutz Medical campus under a 14-hour light:10-hour dark cycle, at 22.2ºC +/- 1.1ºC with 40% +/- 10% humidity. Mice were fed with a standard ad libitum diet (2920X, Teklad, Inc. USA) and watered with hyperchlorinated water (2 - 5 ppm). All mice were handled and cared for following accepted National Institute of Health guidelines. All experiments were conducted with the approval of the University of Colorado Anschutz Medical Campus Institutional Animal Care and Use Committee (IACUC protocol # 01262).

Fetal tissue collection. All tools were disinfected with 70% ethanol and sprayed with RNaseZap (Invitrogen, USA) before use. 1X phosphate buffered saline without calcium or magnesium (PBS -/-) was made using H_2O with diethyl pyrocarbonate (DEPC-H_2O) to prevent RNase activity during sample procurement. At the desired gestational age, pregnant dams were euthanized by the isoflurane drop method followed by cervical dislocation per university approved IACUC protocol #01262. Embryos were harvested into 1X DEPC-PBS -/- on ice. Both ovary / mesonephros complexes from each female embryo were quickly dissected and added to a droplet of optimal cutting temperature compound (OCT) on a petri dish. This allowed removal of excess DEPC-PBS before transferring ovary-mesonephros complexes to a cryomold. Our goal was to place as many ovary/mesonephros complexes as possible into one cryomold (**Fig. 1**). Thus, two pregnant dams were used for E12.5, E16.5, and E18.5, and three pregnant dams were used for E14.5. At least two pregnant dams were necessary for these embryonic stages due to the size of the ovaries and the necessity of preparing multiple cryoblocks to maximize the chance of obtaining a section worthy of sequencing. Dissections were performed in under 20 minutes to minimize RNA degradation.

Perinatal and adult tissue collection. For fetal dissections, all tools and dishes were first disinfected with 70% ethanol and sprayed with RNaseZap. All 1X PBS-/- was prepared using DEPC-H_2O to further prevent RNase activity during dissection. For perinatal dissections i.e. postnatal day 0 (P0) and P3, pups were anesthetized with isoflurane followed by decapitation and bisection. The lower bisected half was added to 1X DEPC-PBS -/- on ice. Ovary/oviduct complexes were quickly excised and added to a droplet of OCT. For P21 and P90, animals were euthanized using the isoflurane drop method followed by decapitation or cervical dislocation. Ovary/oviduct complexes were collected in a pool of 1X DEPC-PBS to wash off excess blood and then added to a droplet of OCT. Dissections were performed in under 10 minutes to protect RNA quality.

Cryoblock preparation. Blocks were prepared with the express goal of adding as many ovaries as possible to a single mold, ideally in the same plane, to maximize the sequencing potential for each time point. To accomplish this, the ovaries that were previously added to an OCT droplet (see above) were individually removed and added side-by-side to the bottom of a 7 mm x 7 mm cryomold. See **Figure 1** for an example block that was fully loaded. Care was taken to make sure that the ovaries were in different orientations such that when a cut was made through a plane the section would contain different representative planes through the ovary. Once the ovaries were added to the block and the space was maximally filled, OCT was carefully added slowly to the mold using a syringe, filling it to the top. If the ovaries shifted, they were carefully pushed back to the bottom with forceps to avoid introducing bubbles. The mold was then flash frozen using a dry ice / 100% ethanol bath. The dry ice bath was allowed to cool for at least 10 minutes before use. Flash frozen blocks were then transferred to a -80ºC freezer for storage until ready to be sectioned. If there were leftover ovaries, additional blocks were made until all tissue was used.

Cryosectioning. Sectioning was performed as described in 10X Genomics Visium HD *Fresh Frozen Tissue Preparation Demonstrated Protocol* (CG000763 Rev A). Briefly, 10-µm sections were cut using a Leica cryostat (Leica Biosystems, USA) set to -20ºC. Blocks were equilibrated to the cryostat chamber temperature

for at least 30 min before sectioning. Blocks were mounted with the part of the block containing the samples facing out toward the user. The cryostat blade was changed before each session, and slides were equilibrated to the chamber temperature prior to sectioning. Blocks were mounted in a mound of OCT and allowed to freeze for 2 min before mounting the chuck on the section head. Sections were cut at 10-µm intervals, and each section was captured onto a slide. To adhere a section to the slide, the flat section was gently touched with the front of a blank slide, and the OCT was melted using a finger pressed to the back of the slide. Once completely melted, the section was then added back to the cryobar and allowed to re-freeze. Two consecutive sections were placed on each slide. Slides were stored at -80ºC.

Hematoxylin and Eosin (H&E) staining and imaging. Methanol fixation and H&E staining was performed in accordance with 10X Genomics *Visium CytAssist Spatial Gene Expression for Fresh Frozen Demonstrated Protocol* (CG000614 Rev A). This protocol was used because present day fixation procedures had yet to be released (see CG000763 Rev D). Following staining, slides were imaged at 20X using a Leica DM6b microscope (Leica Microsystems, USA), images were captured using a Leica K3C camera, and images were processed and stitched using LAS-X software. Downstream tissue processing was performed by the University of Colorado Anschutz Genomics Shared Resource (RRID: 021984).

cDNA library preparation and sequencing. Sections were hybridized overnight with 10x Genomics' whole transcriptome probe pairs following the *Visium HD Spatial Gene Expression Reagent Kits User Guide* (CG000685 Rev B). After washing and ligation of bound probe pairs, the prepared slide and a Visium HD slide were processed on the CytAssist instrument to transfer and spatially barcode the ligated probes. Spatially barcoded products underwent library preparation per the Visium HD protocol. Libraries were pooled and sequenced on an Illumina NovaSeq X Plus system (150bp x 10bp x 10bp x 150bp) at the University of Colorado Genomics Shared Resource (RRID: 021984), generating approximately 500 million reads per capture area.

Spatial transcriptomics data analysis. Loupe Browser (version 8.1.2) was used to manually outline tissue sections for the E12.5 and E14.5 datasets to exclude one testis and one adrenal gland present on those slides (see yellow asterisks in **Figure 2**). For the remaining datasets, tissue detection was performed automatically by SpaceRanger (10X Genomics, USA). Raw data were processed using SpaceRanger (version 3.1.2). SpaceRanger outputs data at the level of the 2 µm detection spots present on the Visium HD slide. Due to the sparsity of the 2 µm data, SpaceRanger also bins the 2 µm data into larger squares tiled across the capture area. Unless otherwise noted, downstream analysis was performed using 8 µm square bins, which provided the optimal tradeoff between spatial resolution, quality of cell type identification from clusters, and computational performance.

Integration and clustering were performed using Seurat[41] (version 5.1.0). 8 µm bins with fewer than 50 reads were filtered out and data were log-normalized. To facilitate efficient clustering of such a large dataset, we used sketch-based sampling to select 50,000 8 µm bins for each stage while preserving rare cell types[42]. This subset was used to perform variable feature selection, data scaling and principal component analysis (PCA). Integration of data from the different fetal and postnatal stages was performed using Seurat's reciprocal PCA method. 8 µm bins were clustered using graph-based clustering (30 principal components, resolution = 0.8). Integration and clustering were projected onto the full dataset. Differential gene expression was used to identify marker genes for each cluster. *De novo* and known marker genes were used alongside the spatial positions and distributions of each cluster to perform cell type identification.

Although 8 µm binning performs better for clustering and cell-type annotation, the 2 µm data provide better spatial resolution for the visualization of individual genes. To reduce the sparsity of the 2 µm data while retaining the high spatial resolution, we utilized SAINSC (version 0.3.1) to perform kernel density estimation (KDE) on the 2 µm data, providing high-resolution, smoothed gene expression profiles for visualization[43]. SAINSC was also used to assign cell types to 2 µm bins.

***Data visualization*.** Visualizations of expression data and clusters projected onto the tissue image were generated using SpatialData (version 0.3.0) and Matplotlib (version 3.10.0)[44,45]. Additional graphs were generated with ggplot2[46] (version 3.5.2). Plotgardener[47] (version 1.14.0) was used for assembling figures.

***Data and code availability*.** Sequencing data have been deposited in the Gene Expression Omnibus (GEO) and will be made public upon peer-reviewed publication, and shared upon reasonable request in the meantime. All analysis code is available on GitHub: https://github.com/McKeyLab/Ovary_VisiumHD.

Technical Validation

Overview of Histology. To generate a comprehensive dataset of ovarian development while maximizing use of the Visium HD slide (10X Genomics, USA) area we utilized a high density, multi-orientation embedding strategy. For each timepoint multiple ovaries were co-embedded on either the dorsal or ventral side in a single cryomold. This approach produced sections containing several ovarian profiles, each of which were sectioned at different planes in the dorsal-ventral axis. The inclusion of peripheral tissues, namely the oviduct, the uterus, and the rete ovarii, further allowed for the preservation of key contextual structures. This helps determine orientation of each individual ovary and provides a more complete view of gene expression in the developing ovary in relation to other reproductive tract components. An overview of all eight sections used for sequencing is provided in **Figure 2**. For capture of detailed tissue morphology and alignment of transcriptomic data, a dual imaging approach was implemented (**Fig. 2a, b**; *top and middle rows*). Low resolution images of the H&E-stained sections were captured by the CytAssist instrument (10X Genomics, USA) and were used for spatial alignment of transcriptomic data in SpaceRanger (10X Genomics, USA) (**Fig. 2a, b**; *top rows*). While useful for alignment, these images did not capture detailed resolution of tissue morphology. To address this, 20X magnification images of the H&E-stained sections were acquired for each stage prior to sequencing (**Fig. 2a, b**; *middle rows*). Assessment of tissue morphology shows that some of the ovarian tissue was fragmented or folded – a common artifact in fresh frozen tissue sections. However, in all eight timepoints at least two ovaries were captured with intact tissue morphology. The number of ovaries captured per section differed between the time points, with fetal tissue containing as many as 10 ovaries with good quality morphology (**Fig. 2a**). Postnatal timepoints had the most variability in size with 11 ovaries captured at P0 and two complete ovaries captured at P90 (**Fig. 2b**). Despite the tissue artifacts from sectioning, projection of the integrated cell clusters onto tissue successfully resolved distinct spatially regionalized cell subtypes both within the ovary and in peripheral tissue, confirming the validity of our approach (**Fig. 2a, b**; *bottom rows*).

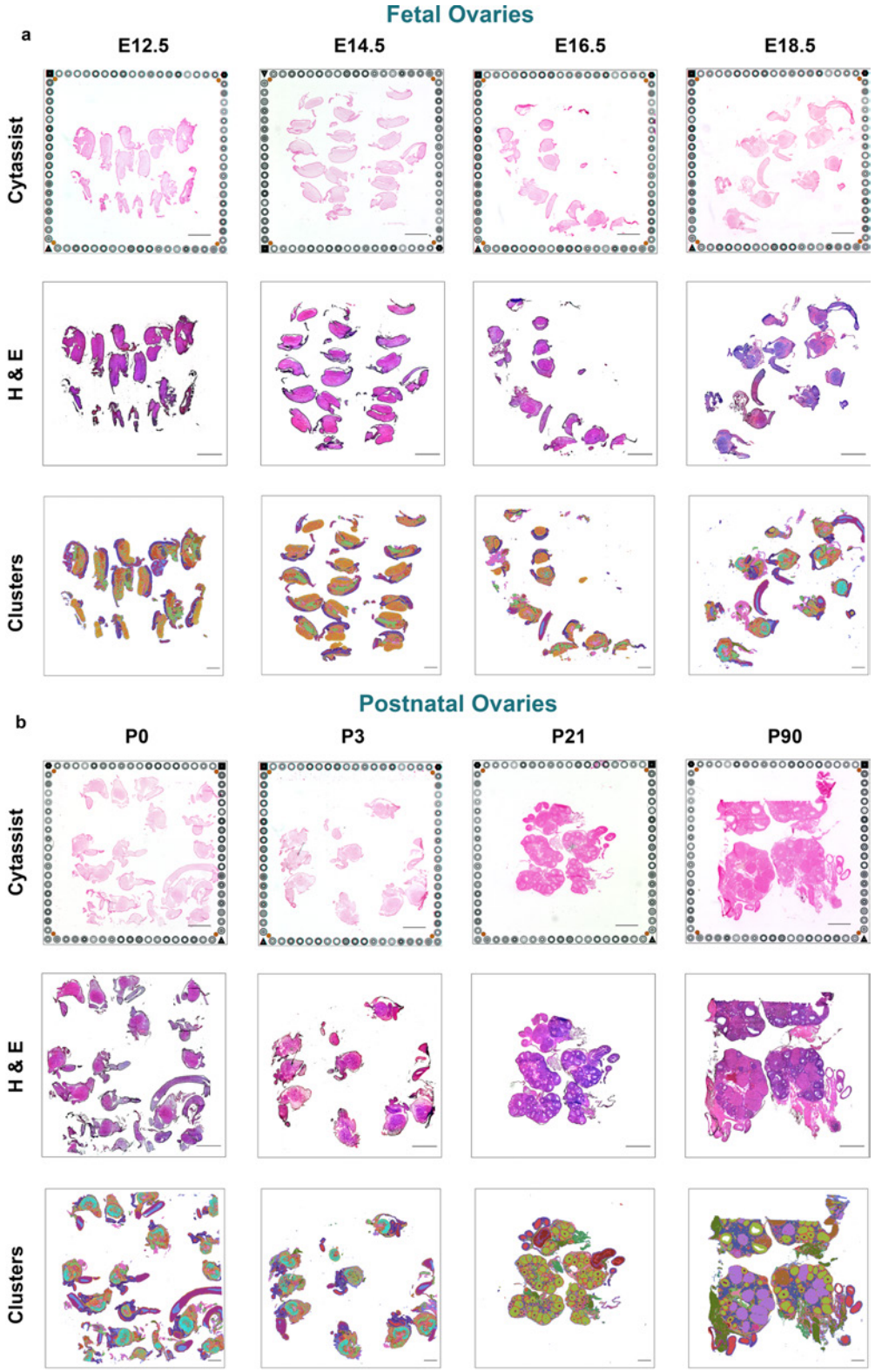

Figure 2. **Tissue processing and cluster projection**. (**a-b**) *Top row*: CytAssist image obtained prior to sequencing and subsequently used for alignment of capture areas to regions of tissue. Scale bars, 1000 µm. *Middle row*: 20x high resolution images of H&E stains pre-sequencing. Scale bars, 1000 µm. *Bottom row*: Projection of 34 clusters identified in the integrated spatial dataset onto the tissue for each timepoint. Scale bars, 1000 µm. (**a**) Fetal stages: E12.5, E14.5, E16.5 and E18.5. Yellow asterisks indicate tissue sections that were excluded from further analysis: a testis at E12.5 and an adrenal gland at E14.5. (**b**) Postnatal stages: P0, P3, P21, P90.

Sequencing quality control. To assess the quality of our sequencing data, we displayed and quantified the number of unique molecular identifiers (UMIs) and genes detected in each 8 µm capture area for each of the eight timepoints (**Fig. 3**). Projecting UMI counts onto the tissue provided critical insight into spatial context of UMI counts across the sectioned tissue as well as identification of technical artifacts in tissue structures (**Fig. 3a-h**). UMI counts were spatially enriched in the ovarian domains relative to surrounding tissue, particularly at late fetal and early perinatal stages (E16.5 to P3; **Fig. 3c-f**). By late postnatal stages (P21 and P90; **Fig. 3g, h**), high UMI counts were concentrated in growing follicles nearest the cortex, which is consistent with increased transcriptional activity associated with primordial follicle activation and subsequent stages of early folliculogenesis. Spatial analysis of UMI counts also revealed tissue-level artifacts, such as folds that create artificially dense areas of UMI counts, as well as incomplete sections where tissue integrity was compromised (P0, **Fig. 3e**). These data demonstrate the power of spatially based QC to assess data quality on a local, per-ovary basis beyond global distributions alone. To complement these spatial projections, we also quantified global UMIs and n(genes) for each timepoint (**Fig. 3i, j**). Across all eight time points, the data show robust transcript capture, with the majority of 8 µm capture areas containing between 1,000 and 5,000 UMIs. E16.5 exhibited the highest transcriptional complexity, having both the highest median UMI count as well as the maximum detected value, which exceeds 15,000 UMIs in some 8 µm capture areas. This could indicate high transcriptional activity, as E16.5 corresponds to the period in ovary organogenesis where germline cysts begin to fragment prior to follicle formation[19,48]. However, this could also simply reflect robust tissue capture and

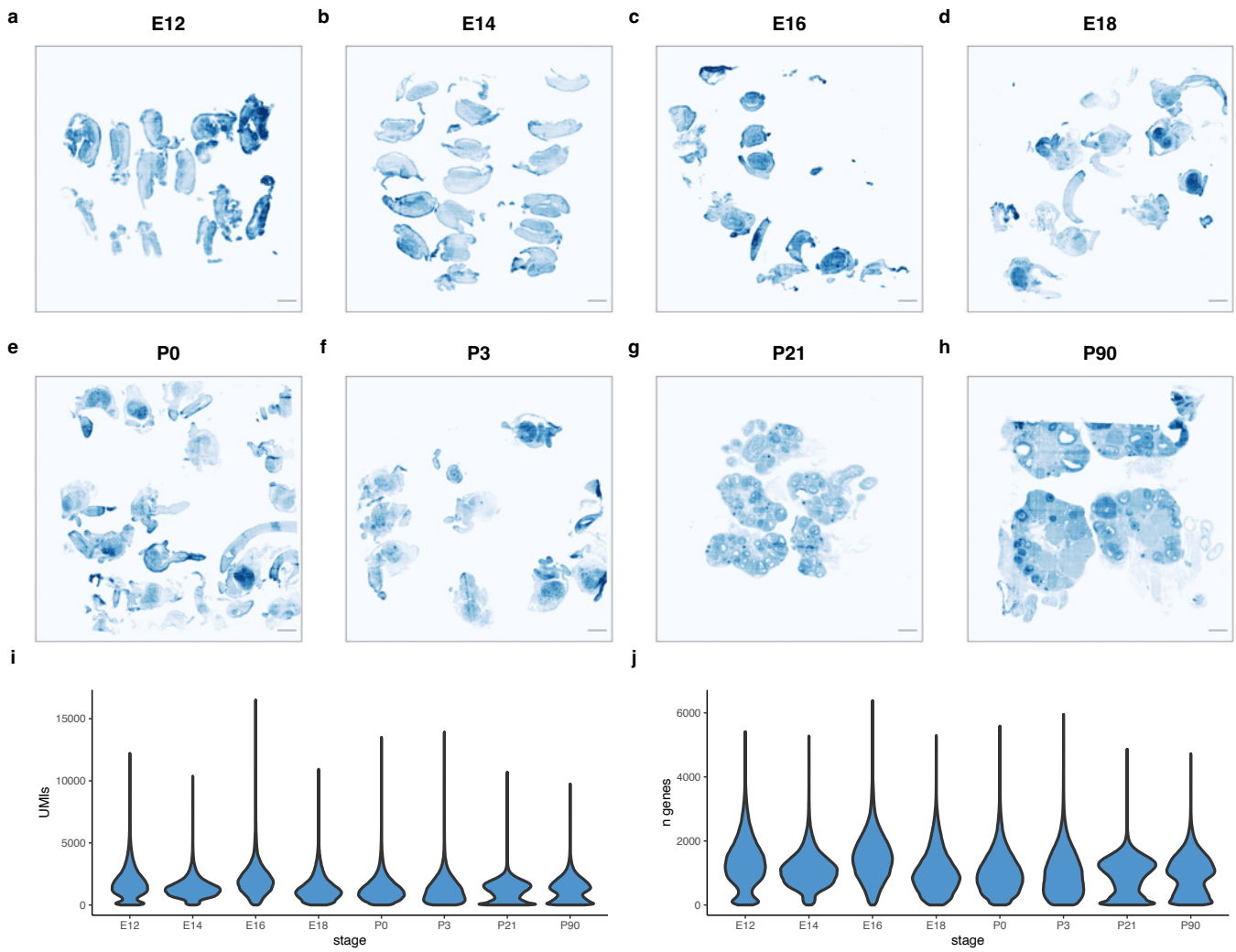

Figure 3. **Technical validation of UMI complexity and gene capture**. (**a – h**) UMI counts for each timepoint projected onto histology images of the sequenced tissue: (**a**) E12.5, (**b**) E14.5, (**c**) E16.5, (**d**) E18.5, (**e**) P0, (**f**) P3, (**g**) P21, (**h**) P90. Scale bars, 500 µm. (**i**) Violin plot showing distribution of UMI counts per capture area for each timepoint. (**j**) Violin plot showing the distribution of the number of genes detected per capture area at each stage.

sequencing at this stage relative to the other timepoints. Subsequent stages from E18.5 to P3 displayed relatively stable UMI distribution between timepoints. Notably, the later postnatal timepoints (P21 and P90) developed a bimodal distribution of UMIs, consistent with the heterogeneity of UMIs observed in the spatial projections (**Fig. 3g, h**). These observed trends in UMI distributions across developmental timepoints are strongly corroborated by the number of genes detected per each 8 µm spot, which mirrored the UMI count distributions across all eight stages (**Fig. 3j**). Together, the quantitative assessment of UMIs and captured gene distributions along with spatially assessed UMI counts confirm that our data capture high quality transcriptomes of the developing mouse ovary. These data further reflect the capture of both key biological processes and identifiable technical features, validating the robustness of our dataset for further investigation.

Cell type annotation of integrated spatial clusters. To create a computationally manageable dataset for analysis, we subsampled 50,000 8 µm capture areas from each of the eight timepoints, yielding a combined pool of 400,000 8 µm capture areas. We then integrated these data using Seurat's reciprocal PCA method, and performed graph-based clustering, which identified 34 distinct cell subtypes (**Fig. 4a**). Clusters were annotated using a combination of spatial distribution of known marker genes, co-localization of marker gene expression with generated clusters, and assessment of differentially expressed gene profiles. For example, oocytes were identified with canonical markers *Ddx4* and *Dazl*. Meiotic, quiescent primordial and active oocyte clusters were differentiated using spatial gene expression of *Stra8*, which marks entry into meiosis (fetal)[30,38], *Sohlh1*, a marker of primordial oocytes[28], and *Zp3* which becomes expressed in oocytes of primary follicles (postnatal)[49]. Differential gene expression analysis using Loupe Browser 8 (version 8.0.0) showed that the presumptive meiotic cluster displayed up-regulation of meiotic entry genes like *Tex12, Meioc, Sycp3,* and *Sycp1* at E14.5, whereas the presumptive active oocyte cluster had up-regulation of genes associated with more mature oocytes at P21 and P90 such as *Oosp3, Sgo2b,* and *Nlrp4e* and *Zp3*, confirming our initial annotation of these clusters. This same approach was used with other markers such as *Nr5a2* and *Up3kb,* which were used to identify active granulosa and ovarian surface epithelium clusters respectively. Beyond ovary-specific cell types, canonical markers for vascular (*Emcn*, *Pecam1*), immune (*Adgre1*, *Cd86, Cd68*) and lymphatic (*Prox1*, *Lyve1*) components were used to distinguish between these spatially similarly distributed clusters. A comprehensive list of the markers used for preliminary identification of cell types is presented in **Table 1**. The combination of spatial gene expression, spatial localization of the clusters and enriched genes in each cluster allowed for robust and complete annotation of our dataset.

Cell type	Markers
Active Granulosa Cell	*Cyp19a1, Amh, Fshr, Nr5a2*
Active oocyte	*Zp3, Bmp15, Gdf9*
Adipocyte	*Lep, Adipo1, Fabp4, Adipoq*
Corpus Luteum	*Oxtr, Ptgfr, Lhcgr, Star,Fdx1*
Early Antral Granulosa	*Inhba, Inhbb*
Endothelial	*Pecam1, Cldn5, Emcn*
Granulosa Cell	*Foxl2, Runx1, Kctd14, Fst*
Lymphatic vessels	*Prox1, Lyve1*
Macrophage	*Adgre1, Cd68, Cd86*
Meiosis	*Stra8, Rec8, Sycp3*
Mesothelial Cells	*Msln, Up3kb, Lrrn4*
Müllerian duct / oviduct / uterus	*Ovgp1, Mecom, Pgr, Wnt7, Pax8, Pax2*
Oocyte	*Ddx4, Dazl, Figla, Mael, Sycp3, Sohlh1*
Ovarian Surface Epithelium	*Upk3b, Lgr5, Lhx9, Gng13, Krt19*
Pre-meiotic germ cell	*Nanog, Dnd1, Dmrt1*
Preantral Granulosa	*Kctf14, Gas6*
Rete ovarii	*Pax8, Gfra1, Rnase12, Slc25a21, Lypd1, Pax2*
Smooth Muscle	*Acta2, Tagln, Cnn1, Myh11*
Stroma	*Nr2f2, Arx, Dcn, Lum, Col1a1, Col6a1, Pdgfra, Col1a2*
Theca Cell	*Cyp17a1, Cyp11a1, Gli1*

Table 1. List of cell type markers used to guide cluster annotations.

In addition to robust annotations, the integration of the dataset identified clusters present only at specific stages of ovarian development. For instance, at E12.5 many genes specific to the adrenal medulla were identified in one of the clusters. This is in line with the fact that the adrenal primordium and gonad have not yet fully separated at this stage[39], and it is challenging to dissect the ovary without carrying over the adrenal primordium. As expected, this cluster is only represented at this early fetal timepoint (**Fig. 4b**). In contrast, the early and late corpus luteum (CL) clusters were represented only at P90 (*larger yellow bar* in **Fig. 4b).** This is consistent with CLs being a post-ovulatory endocrine structure, and with the first ovulation typically occurring after P21 in CD-1 mice. Of note, we found a small proportion of spots in P21 ovaries assigned to the

“corpus luteum late” cluster (1% of total spots), which we hypothesize is a sign of follicle atresia, as spatial evaluation showed that these spots were found in smaller, collapsed follicles in these samples.
To assess whether the generated clusters were also spatially patterned in a biologically significant manner we projected the clusters onto the tissue (**Fig. 4c-j**). Spatial projection of the 34 identified clusters revealed clear, specific, and highly resolved patterning. Clear boundaries between the ovary and peripheral tissue are discernible with the ovarian domain, mesonephros, and oviduct displaying distinct patterning of non-overlapping clusters. Not only were these data able to discern specific regions and cell types of the ovary based on transcriptomic profiles, but also the integrated dataset captured changing transcriptional patterns in the ovary itself across time. At E12.5 and E14.5 the ovarian domain is populated with *early granulosa*, *pre-granulosa/oocyte mix*, and *meiotic oocyte* clusters (**Fig. 4c, d**). By E16.5, the *primordial oocyte* cluster was starting to be represented (**Fig. 4e**), and by E18.5 spots assigned to this cluster were densely scattered across

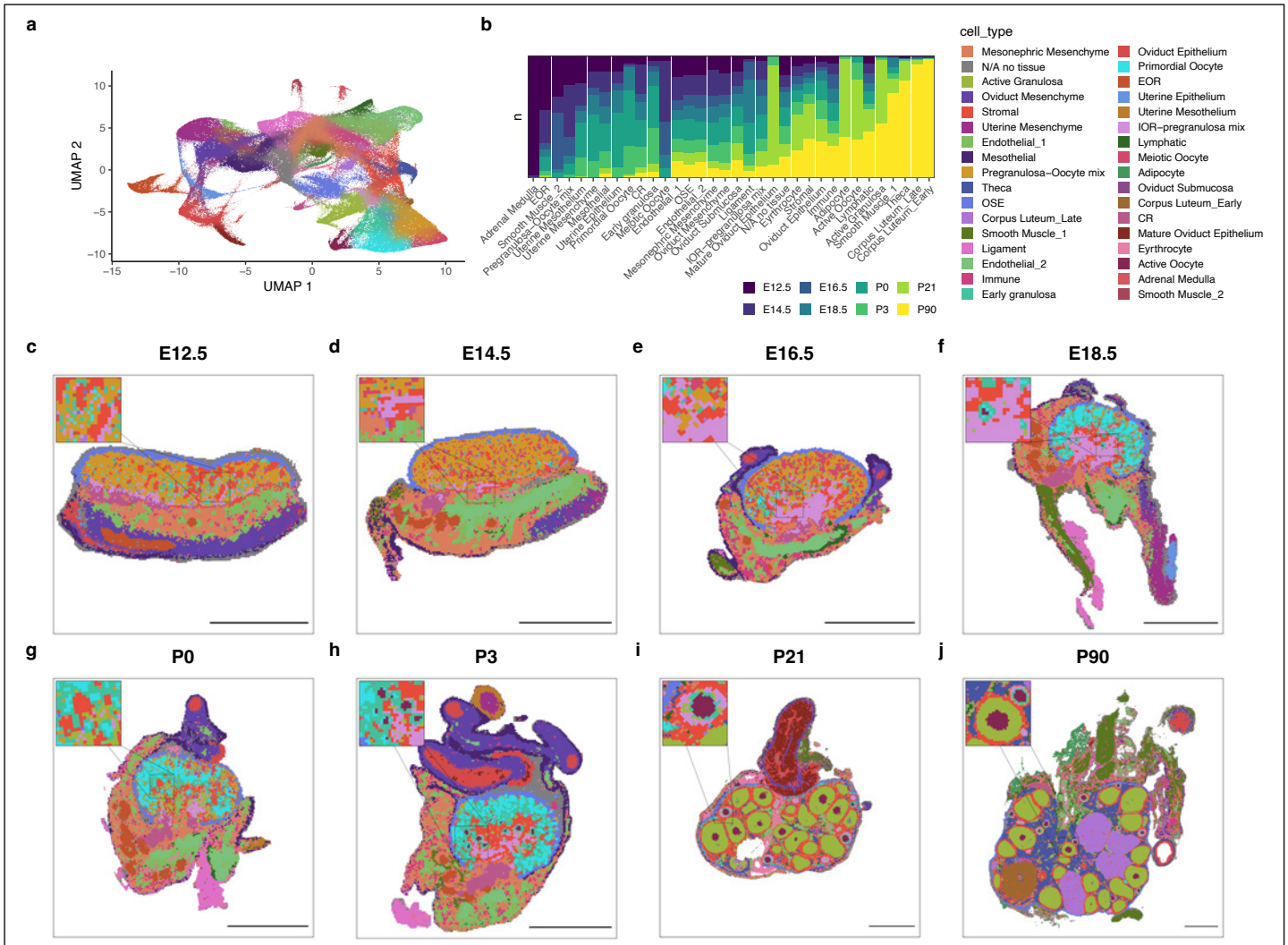

Figure 4. **Integrated clustering of the full dataset**. (**a**) UMAP projection of 34 clusters identified using integration of 400,000 subsampled 8 µm bins across all eight timepoints. *Abbreviations*: OSE, ovarian surface epithelium; IOR, intraovarian rete; CR, connecting rete; EOR, extraovarian rete. (**b**) Bar plot depicting proportion of 8 µm bins assigned to each cluster at each stage. “Cell type” displays the 34 annotated clusters used in the UMAP and cluster projections. (**c – j**) Projections of the 34 identified clusters from the integrated dataset onto individual ovaries from each timepoint: (**c**) E12.5, (**d**) E14.5, (**e**) E16.5, (**f**) E18.5, (**g**) P0, (**h**) P3, (**i**) P21, (**j**) P90. The insets in the top left corner show blow-ups of a region within the image, illustrating the high spatial resolution of the clusters. Clipping masks were applied to the background to isolate each ovary from the rest of the image. *Scale bars, 500 µm*.

the cortex (**Fig. 4f**) highlighting the regionalization into medullary and cortical domains that persists until P3 (**Fig. 4g, h**). By P21 and P90 most of the previously observed clusters had disappeared and were replaced

with clusters associated with the mature ovary, namely: active granulosa cells, active oocytes, and corpus luteum (**Fig. 4i, j**). Of note, we opted to name the clusters based on the ultimate outcome of the cell types. Since all stages were integrated together, our cluster annotations might in some cases be confusing, as spots from the same clusters represent the final differentiated cell type in the older stages, but their progenitors in the early fetal stages. An example of this is the extraovarian rete cluster (EOR), which at E12.5 and E14.5 captures the Wolffian duct and mesonephric tubules. Because these cells ultimately become the EOR, we chose to label the cluster "EOR".

Moreover, the mapping of the integrated cluster data spatially overlapped with high precision to the underlying tissue itself, indicating that alignment between the spatial coordinates of each bin mapped with high fidelity to its tissue origin. Together these data indicate that the subsample used for generation of the integrated spatial transcriptomic dataset robustly captured diverse cell subtypes present across ovarian development, that our cluster annotations accurately identify ovarian cell subtypes, and that integration allowed for identification of cell subtypes uniquely represented at specific points of time during murine ovarian development. This spatial dataset also displays with unprecedented detail the association between unique gene expression signatures and spatial patterning of ovarian cell subtypes.

An* in-situ *gene expression library at 2 µm resolution. Our annotation strategy went beyond sole reliance on a few marker genes for cluster identification, by integrating gene expression with spatial localization. This approach allowed for robust cell type identification within the integrated dataset. To demonstrate the power of this approach for discovery, we performed differential analysis of the top two enriched genes for each cluster using the *FindAllMarkers* function of Seurat (**Fig. 5a**). The resulting heatmap identified cell-type makers not traditionally associated with these annotations, but which were identified using an unbiased empirical approach. The integrated spatial framework thus enables the discovery of novel transcriptional signatures across ovarian development worthy of further investigation. This approach also confirmed that the clustering of our spatial data yielded highly resolved gene expression signatures (**Fig. 5a**).

One major advantage of spatial transcriptomics is the ability to observe gene expression *in situ* at near single-cell scale in the context of the tissue: the integrated spatial dataset is in essence a near transcriptome-wide *in situ* gene expression library that one can query for almost every gene expressed during ovarian development. The smallest unit of resolution provided by the Visium HD platform is 2 µm x 2 µm sized bins which offer near single cell resolution. Ordinarily, these data are too sparse to allow reasonable evaluation of spatially-resolved gene expression (**Fig. 5b-d**). However, we overcame this limitation by applying kernel density estimation using SAINSC to fit a Gaussian kernel to the 2 µm expression data. This approach provides smoothed 2 µm expression profiles that provide higher resolution mapping of gene expression profiles than could be achieved with the 8 µm bins, as seen for example with *Dazl* expression in adult oocytes (Fig. 5b-e).

Figure 5 f-i illustrates the strength of this dataset for querying gene expression by illustrating the expression of four marker genes at E18.5: *Dazl* (oocytes), *Pax8* (rete ovarii and reproductive tract epithelium), *Foxl2* (pre-granulosa cells), and *Up3kb* (ovarian surface epithelium). The expression of each marker is localized to highly distinct domains where expression is expected to occur: *Dazl* highlights the ovarian cortex where most oocytes are localized at E18.5 (**Fig. 5f**), *Pax8* is localized to the rete ovarii and oviduct epithelia (**Fig. 5g**), *Foxl2* is localized to the ovarian domain (**Fig. 5h**) and *Up3kb* is localized to the surface of the ovary and surrounding tissue (**Fig. 5i**). These are just four selected genes displayed on a single ovary from one timepoint. The total dataset contains eight different time points with – in some cases – nearly a dozen ovaries per section, each of which were sectioned at differing planes, unlocking a wealth of potential information.

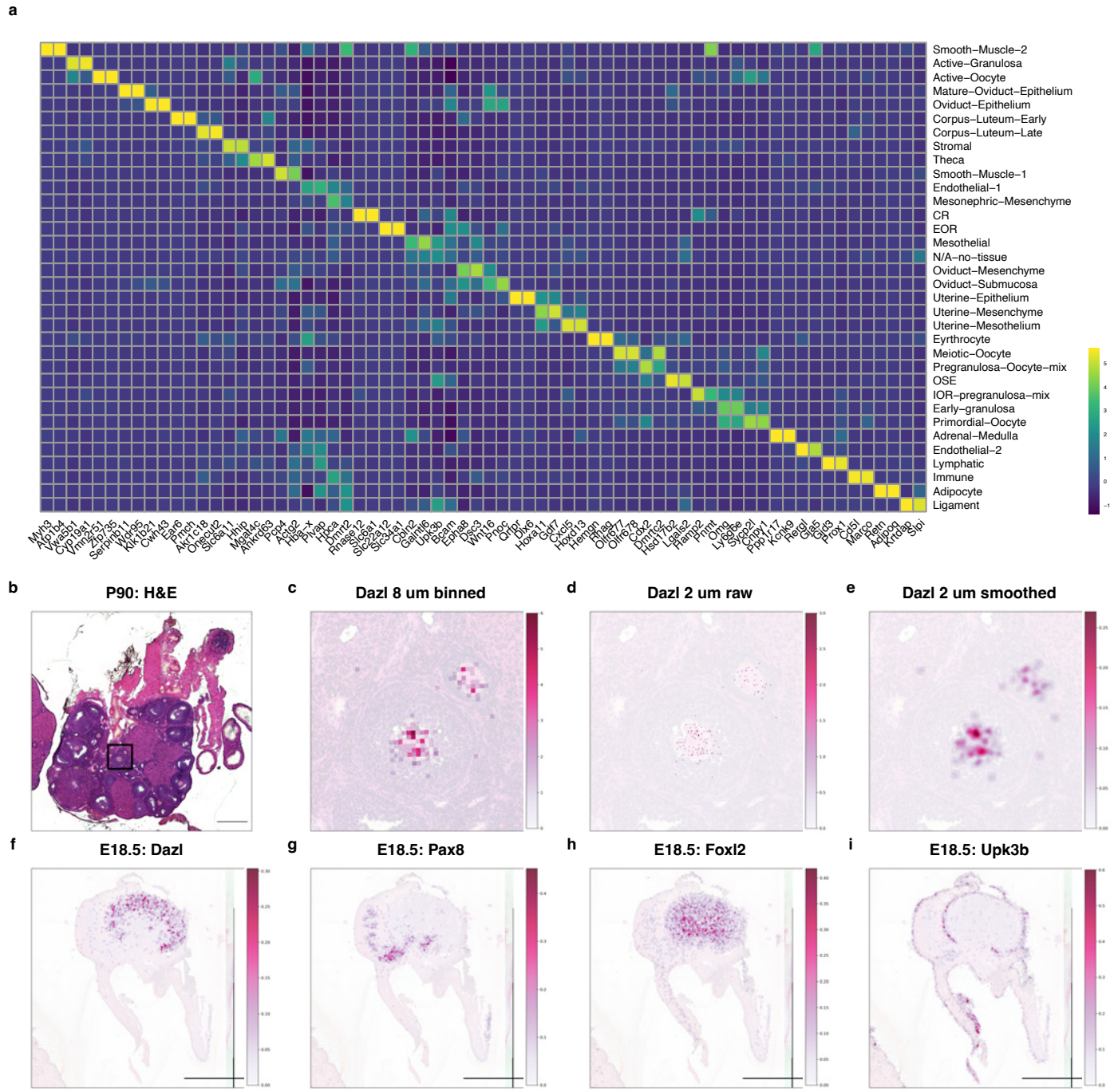

Figure 5. (**a**) Heatmap displaying the 34 integrated clusters along with their top two uniquely expressed genes. Yellow indicates higher expression, blue indicates lower expression. (**b** - **e**) Comparison of the spatial resolution of gene expression between the 8 µm bins and the 2 µm bins smoothed using SAINSC on the P90 sample to display expression of the oocyte marker *Dazl*. (**b**) H&E of full section; (**c-e**) Close-up image of the two follicles outlined in the black box in (**b**) showing *Dazl* expression in the oocytes using 8 µm bin resolution (**c**); using raw 2 µm bin resolution (**d**); or using the 2 µm SAINSC-smoothed expression (**e**); (**f - i**) Spatial gene expression of four marker genes at E18.5: (**f**) *Dazl* labels oocytes, (**g**) *Pax8* labels the rete ovarii, (**h**) *Foxl2* labels granulosa cells, (**i**) *Upk3b* labels the ovarian surface epithelium and the surface of mesonephros-derived tissue.

Limitations of the study

While the strengths and power of this dataset are described above, we must also mention several limitations of our spatial transcriptomics study. First, while 2 µm and 8 µm bins provide extremely high resolution for spatial evaluation of gene expression, cells in the fetal ovary are so densely packed that some clusters were inevitably composed of mixed cell types. For example, in most fetal stages, individual spots on

the Visium HD slide bordered both germ cells and pre-granulosa cells, leading to the mixed “oocyte-pre-granulosa cell mix” cluster. Since we were able to use the 2 µm bins to visualize smoothed gene expression, we did not consider this to limit the analysis and interpretation needed for this report.

Second, the tissue histology was not always interpretable. This was especially limiting for the evaluation of the ovarian surface epithelium. Because our H&E images were captured before RNA:probe hybridization, we could not use mounting media, thus sections began to dry at the edges, producing a grainy appearance. This also limited the resolution of the tissue, making it sometimes difficult to distinguish larger oocytes from pre-granulosa cells in fetal stages and in primordial follicles of the postnatal stages. This might have been improved if we had chosen to use paraffin embedding instead of cryosections, as paraffin better preserves tissue histology. However, we chose to optimize for quantity and multi-orientation of samples, and cryo-embedding was the only way we could ensure that many ovaries would be embedded in the same block on the same sectioning plane. Nonetheless, RNA capture and sequencing quality were excellent across the entire sections, including edges, thus the clustering and gene expression were still optimal, even for the surface epithelium and smaller follicles.

Third, because we used the *HD whole transcriptome panel gene expression* version of the Visium HD slide which is probe-based, only transcripts for protein-coding genes were sequenced, and the slide does not provide 100% transcriptome coverage (~19,059 genes targeted by 55,187 probes). This means our dataset cannot be used to explore isoform expression, and some genes are missing from our dataset. For example, the expression of *Slc18a2*, a recently identified marker of the transition from pre-granulosa to granulosa cells[34,50], is not found in our dataset. While we found that the default coverage was more than sufficient for our study, this could have been prevented by custom-designing probes to add genes of interest that were not represented in the default workflow. Of note, 10X Genomics recently released a *Visium HD 3’ gene expression* workflow that allows whole transcriptome sequencing, including isoforms, and is species-agnostic.

Finally, the intrinsic sparseness of spatial sequencing along with the sheer volume of the data, make it difficult to efficiently implement popular downstream analysis tools, such as ligand-receptor interaction or transcription factor activity analysis. This is a rapidly evolving field, and we are certain that these tools will soon be accessible with HD spatial transcriptomics data. In the future, applying these approaches to a representative subset of spatial spots, and adapting approaches that were developed for other spatial platforms may yield interesting insights into these datasets.

Conclusion

In summary, we provide a high quality comprehensive integrated spatial transcriptome of the mouse ovary spanning fetal, perinatal, juvenile and adult stages at near single cell resolution. In addition, to the best of our knowledge, this is the first time-course dataset that includes not only the ovary, but also surrounding tissues, such as the mesonephros (early fetal), reproductive tract (all stages), ligaments (all stages), adipose tissue (adult), and rete ovarii (all stages). This will enhance our ability to explore functional interaction between the ovary and adjacent cell types. Our goal is to make this dataset user-friendly and accessible, so that it may serve as a resource for the field. This will help advance our global understanding of the molecular mechanisms driving spatial patterning of all ovarian cell types, which will uncover novel determinants of female fertility and potential therapeutic targets to combat female subfertility and ovarian disease.

Acknowledgements

This study was supported by start-up funds from the CU Anschutz Medical Campus, School of Medicine, Department of Pediatrics, Section of Developmental Biology to JM, and by funding from the National Institutes of Health to JM (grant #R00HD103778). This study was supported in part by the University of Colorado Anschutz Medical Campus Genomics Shared Resource (RRID: 021984). We are grateful to all members of the McKey laboratory and the Roberson laboratory for helpful discussions and suggestions on the work presented here.

Author contributions

ASM designed the experimental pipeline and carried out the experiments; TJG conceptualized the data analysis pipeline and processed and analyzed the data with guidance from ASM and JM for cluster annotation; TJG formatted and deposited the data in appropriate repositories; ASM, TJG and JM drafted, revised and edited the manuscript; JM acquired funding and supervised the project.

Competing interests

The author(s) declare no competing interests.

References

1. Hu YC, Okumura LM, Page DC. Gata4 is required for formation of the genital ridge in mice. PLoS Genet. 2013;9(7):e1003629. PMCID: PMC3708810
2. Bowles J, Koopman P. Precious cargo: regulation of sex-specific germ cell development in mice. Sex Dev. 2013;7(1–3):46–60. PMID: 22947624
3. Stévant I, Nef S. Genetic Control of Gonadal Sex Determination and Development. Trends in Genetics. 2019 May;35(5):346–358.
4. Karl J, Capel B. Sertoli cells of the mouse testis originate from the coelomic epithelium. Dev Biol. 1998 Nov 15;203(2):323–333. PMID: 9808783
5. Yang Y, Workman S, Wilson MJ. The molecular pathways underlying early gonadal development. 2019 Jan 1 [cited 2025 Aug 16]; Available from: https://jme.bioscientifica.com/view/journals/jme/62/1/JME-17-0314.xml
6. Byskov AG. Differentiation of mammalian embryonic gonad. Physiological Reviews. American Physiological Society; 1986 Jan;66(1):71–117.
7. Imaimatsu K, Uchida A, Hiramatsu R, Kanai Y. Gonadal Sex Differentiation and Ovarian Organogenesis along the Cortical-Medullary Axis in Mammals. Int J Mol Sci. 2022 Nov 2;23(21):13373. PMCID: PMC9655463
8. Hacker A, Capel B, Goodfellow P, Lovell-Badge R. Expression of Sry, the mouse sex determining gene. Development. 1995 Jun 1;121(6):1603–1614.
9. Pepling ME, C. Spradling A. Female mouse germ cells form synchronously dividing cysts. Development. 1998 Sep 1;125(17):3323–3328.
10. Lei L, Spradling AC. Mouse primordial germ cells produce cysts that partially fragment prior to meiosis. Development. 2013 May;140(10):2075–2081. PMCID: PMC3640216
11. Niu W, Spradling AC. Mouse oocytes develop in cysts with the help of nurse cells. Cell. 2022 Jul 7;185(14):2576-2590.e12. PMID: 35623357
12. Stévant I, Kühne F, Greenfield A, Chaboissier MC, Dermitzakis ET, Nef S. Dissecting Cell Lineage Specification and Sex Fate Determination in Gonadal Somatic Cells Using Single-Cell Transcriptomics. Cell Reports. 2019 Mar 19;26(12):3272-3283.e3.
13. Capel B. The battle of the sexes. Mech Dev. 2000 Mar 15;92(1):89–103. PMID: 10704890
14. Lin YT, Capel B. Cell fate commitment during mammalian sex determination. Current Opinion in Genetics & Development. 2015 Jun 1;32:144–152.
15. Eppig JJ, Handel MA. Origins of granulosa cells clarified and complexified by waves. Biol Reprod. 2012 Feb;86(2):34. PMID: 21976596
16. Nicholas CR, Haston KM, Pera RAR. Intact fetal ovarian cord formation promotes mouse oocyte survival and development. BMC Developmental Biology. 2010 Jan 8;10(1):2.
17. Smith P, Wilhelm D, Rodgers RJ. Development of mammalian ovary. 2014 Jun 1 [cited 2025 Aug 14]; Available from: https://joe.bioscientifica.com/view/journals/joe/221/3/R145.xml

18. Wang C, Zhou B, Xia G. Mechanisms controlling germline cyst breakdown and primordial follicle formation. Cell Mol Life Sci. 2017 Feb 14;74(14):2547–2566. PMCID: PMC11107689

19. Pepling ME, Spradling AC. Mouse ovarian germ cell cysts undergo programmed breakdown to form primordial follicles. Dev Biol. 2001 Jun 15;234(2):339–351. PMID: 11397004

20. Pepling ME. Follicular assembly: mechanisms of action. Reproduction. 2012 Feb;143(2):139–149. PMID: 22065859

21. Mork L, Maatouk DM, McMahon JA, Guo JJ, Zhang P, McMahon AP, Capel B. Temporal differences in granulosa cell specification in the ovary reflect distinct follicle fates in mice. Biol Reprod. 2012 Feb;86(2):37. PMCID: PMC3290667

22. Niu W, Spradling AC. Two distinct pathways of pregranulosa cell differentiation support follicle formation in the mouse ovary. Proc Natl Acad Sci U S A. 2020 Aug 18;117(33):20015–20026. PMCID: PMC7443898

23. Yin Q, Spradling AC. Three waves of ovarian follicles in juvenile mice [Internet]. bioRxiv; 2024 [cited 2025 Mar 29]. p. 2024.05.30.596686. Available from: https://www.biorxiv.org/content/10.1101/2024.05.30.596686v2

24. Ng A, Tan S, Singh G, Rizk P, Swathi Y, Tan TZ, Huang RYJ, Leushacke M, Barker N. Lgr5 marks stem/progenitor cells in ovary and tubal epithelia. Nat Cell Biol. 2014 Aug;16(8):745–757. PMID: 24997521

25. Jiménez R. Ovarian Organogenesis in Mammals: Mice Cannot Tell Us Everything. Sex Dev.

26. McKey J, Anbarci DN, Bunce C, Ontiveros AE, Behringer RR, Capel B. Integration of mouse ovary morphogenesis with developmental dynamics of the oviduct, ovarian ligaments, and rete ovarii. Araujo SJ, Stainier DY, editors. eLife. 2022 Sep 27;11:e81088.

27. Hirshfield AN. Heterogeneity of cell populations that contribute to the formation of primordial follicles in rats. Biol Reprod. 1992 Sep;47(3):466–472. PMID: 1511099

28. Zheng W, Zhang H, Gorre N, Risal S, Shen Y, Liu K. Two classes of ovarian primordial follicles exhibit distinct developmental dynamics and physiological functions. Hum Mol Genet. 2014 Feb 15;23(4):920–928. PMCID: PMC3900105

29. Cordeiro MH, Kim SY, Ebbert K, Duncan FE, Ramalho-Santos J, Woodruff TK. Geography of Follicle Formation in the Embryonic Mouse Ovary Impacts Activation Pattern During the First Wave of Folliculogenesis. Biol Reprod. 2015 Oct;93(4):88. PMCID: PMC4711906

30. Soygur B, Gaylord EA, Foecke MH, Cincotta SA, Horan TS, Wood A, Cohen PE, Laird DJ. Sustained fertility from first-wave follicle oocytes that pause their growth [Internet]. bioRxiv; 2024 [cited 2024 Sep 18]. p. 2024.08.27.609995. Available from: https://www.biorxiv.org/content/10.1101/2024.08.27.609995v1

31. Mayère C, Regard V, Perea-Gomez A, Bunce C, Neirijnck Y, Djari C, Bellido-Carreras N, Sararols P, Reeves R, Greenaway S, Simon M, Siggers P, Condrea D, Kühne F, Gantar I, Tang F, Stévant I, Batti L, Ghyselinck NB, Wilhelm D, Greenfield A, Capel B, Chaboissier MC, Nef S. Origin, specification and differentiation of a rare supporting-like lineage in the developing mouse gonad. Sci Adv. 2022 May 27;8(21):eabm0972. PMID: 35613264

32. Wang S, Zheng Y, Li J, Yu Y, Zhang W, Song M, Liu Z, Min Z, Hu H, Jing Y, He X, Sun L, Ma L, Esteban CR, Chan P, Qiao J, Zhou Q, Izpisua Belmonte JC, Qu J, Tang F, Liu GH. Single-Cell Transcriptomic Atlas of Primate Ovarian Aging. Cell. 2020 Feb;180(3):585-600.e19.

33. Frost ER, Ford EA, Peters AE, Lovell-Badge R, Taylor G, McLaughlin EA, Sutherland JM. A New Understanding, Guided by Single-Cell Sequencing, of the Establishment and Maintenance of the Ovarian Reserve in Mammals. Sex Dev. 2023;17(2–3):145–155. PMID: 36122567

34. Taylor G, Frost ER, Crow BN, Radley A, Boeing S, Galichet C, Baker MA, Sutherland JM, Lovell-Badge R. Pregranulosa cells upregulate cardiac troponin I Tnni3 upon cell cycle resumption during primordial follicle activation [Internet]. bioRxiv; 2024 [cited 2024 Sep 24]. p. 2022.10.24.513438. Available from: https://www.biorxiv.org/content/10.1101/2022.10.24.513438v3

35. Garcia-Alonso L, Lorenzi V, Mazzeo CI, Alves-Lopes JP, Roberts K, Sancho-Serra C, Engelbert J, Marečková M, Gruhn WH, Botting RA, Li T, Crespo B, Van Dongen S, Kiselev VY, Prigmore E, Herbert M, Moffett A, Chédotal A, Bayraktar OA, Surani A, Haniffa M, Vento-Tormo R. Single-cell roadmap of human gonadal development. Nature. 2022 Jul 21;607(7919):540–547.

36. Lei L, Spradling AC. Single-Cell Lineage Analysis of Oogenesis in Mice. Methods Mol Biol. 2017;1463:125–138. PMID: 27734353

37. Soygur B, Laird DJ. Ovary Development: Insights From a Three-Dimensional Imaging Revolution. Frontiers in Cell and Developmental Biology [Internet]. 2021 [cited 2023 Sep 8];9. Available from: https://www.frontiersin.org/articles/10.3389/fcell.2021.698315

38. Soygur B, Jaszczak RG, Fries A, Nguyen DH, Malki S, Hu G, Demir N, Arora R, Laird DJ. Intercellular bridges coordinate the transition from pluripotency to meiosis in mouse fetal oocytes. Sci Adv. 2021 Apr;7(15):eabc6747. PMCID: PMC8026130

39. Bunce C, McKey J, Capel B. Concerted morphogenesis of genital ridges and nephric ducts in the mouse captured through whole-embryo imaging. Development. 2021 Sep 15;148(18):dev199208. PMCID: PMC8242465

40. Harikae K, Miura K, Kanai Y. Early gonadogenesis in mammals: significance of long and narrow gonadal structure. Dev Dyn. 2013 Apr;242(4):330–338. PMID: 22987627

41. Hua Y, Weng L, Zhao F, Rambow F. SeuratExtend: streamlining single-cell RNA-seq analysis through an integrated and intuitive framework. Gigascience. 2025 Jan 6;14:giaf076. PMCID: PMC12236070

42. Hie B, Bryson B, Berger B. Efficient integration of heterogeneous single-cell transcriptomes using Scanorama. Nat Biotechnol. 2019 Jun;37(6):685–691. PMCID: PMC6551256

43. Müller-Bötticher N, Tiesmeyer S, Eils R, Ishaque N. Sainsc: A Computational Tool for Segmentation-Free Analysis of In Situ Capture Data. Small Methods. 2025 May;9(5):e2401123. PMCID: PMC12103232

44. Marconato L, Palla G, Yamauchi KA, Virshup I, Heidari E, Treis T, Vierdag WM, Toth M, Stockhaus S, Shrestha RB, Rombaut B, Pollaris L, Lehner L, Vöhringer H, Kats I, Saeys Y, Saka SK, Huber W, Gerstung M, Moore J, Theis FJ, Stegle O. SpatialData: an open and universal data framework for spatial omics. Nat Methods. 2025 Jan;22(1):58–62. PMCID: PMC11725494

45. Hunter JD. Matplotlib: A 2D Graphics Environment. Computing in Science & Engineering. 2007 May;9(3):90–95.

46. Wickham H. ggplot2 [Internet]. Cham: Springer International Publishing; 2016 [cited 2025 Sep 7]. Available from: http://link.springer.com/10.1007/978-3-319-24277-4

47. Kramer NE, Davis ES, Wenger CD, Deoudes EM, Parker SM, Love MI, Phanstiel DH. Plotgardener: cultivating precise multi-panel figures in R. Bioinformatics. 2022 Mar 28;38(7):2042–2045. PMCID: PMC8963281

48. Ikami K, Shoffner-Beck S, Tyczynska Weh M, Schnell S, Yoshida S, Diaz Miranda EA, Ko S, Lei L. Branched germline cysts and female-specific cyst fragmentation facilitate oocyte determination in mice. Proceedings of the National Academy of Sciences. Proceedings of the National Academy of Sciences; 2023 May 16;120(20):e2219683120.

49. Lira SA, Kinloch RA, Mortillo S, Wassarman PM. An upstream region of the mouse ZP3 gene directs expression of firefly luciferase specifically to growing oocytes in transgenic mice. Proc Natl Acad Sci U S A. 1990 Sep;87(18):7215–7219. PMCID: PMC54714

50. Meinsohn MC, Saatcioglu HD, Wei L, Li Y, Horn H, Chauvin M, Kano M, Nguyen NMP, Nagykery N, Kashiwagi A, Samore WR, Wang D, Oliva E, Gao G, Morris ME, Donahoe PK, Pépin D. Single-cell sequencing reveals suppressive transcriptional programs regulated by MIS/AMH in neonatal ovaries. Proc Natl Acad Sci U S A. 2021 May 18;118(20):e2100920118. PMCID: PMC8157966